remote sensing

MDPI

Article

Monitoring Aeolian Erosion from Surface Coal Mines in the Mongolian Gobi Using InSAR Time Series Analysis

Jungrack Kim [1,*], Bayasgalan Amgalan [2] and Amanjol Bulkhbai [3]

[1] Future Vision Inc., Yangpyeong 12523, Gyeonggi-do, Republic of Korea
[2] Mongolian Academy of Sciences, Ulaanbaatar 13330, Mongolia; bayasgalan@iag.ac.mn
[3] National Forest Agency of Mongolia, Ulaanbaatar 16080, Mongolia; amanjol.t@forest.gov.mn
* Correspondence: kjrr001@gmail.com; Tel.: +82-07082533008

Abstract: Surface mining in the southeastern Gobi Desert has significant environmental impacts, primarily due to the creation of large coal piles that are highly susceptible to aeolian processes. Using spaceborne remote sensing and numerical simulations, we investigated erosional processes and their environmental impacts. Our primary tool was Interferometric Synthetic Aperture Radar (InSAR) data from Sentinel-1 imagery collected between 2017 and 2022. We analyzed these data using phase angle information from the Small Baseline InSAR time series framework. The time series analyses revealed intensive aeolian erosion in the coal piles, represented as thin deformation patterns along the potential pathways of aerodynamic transportation. Further analysis of multispectral data, combined with correlations between wind patterns and trajectory simulations, highlighted the detrimental impact of coal dust on the surrounding environment and the mechanism of aeolian erosion. The lack of mitigation measures, such as water spray, appeared to exacerbate erosion and dust generation. This study demonstrates the feasibility of using publicly available remote sensing data to monitor coal mining activities and their environmental hazards. Our findings contribute to a better understanding of coal dust generation processes in surface mining operations as well as the aeolian erosion mechanism in desert environments.

Keywords: coal mine; InSAR; time series analysis; aeolian erosion; dust generation

check for updates

Citation: Kim, J.; Amgalan, B.; Bulkhbai, A. Monitoring Aeolian Erosion from Surface Coal Mines in the Mongolian Gobi Using InSAR Time Series Analysis. *Remote Sens.* **2024**, *16*, 4111. https://doi.org/10.3390/rs16214111

Academic Editor: Salvatore Stramondo

Received: 1 September 2024
Revised: 16 October 2024
Accepted: 28 October 2024
Published: 3 November 2024

Copyright: © 2024 by the authors. Licensee MDPI, Basel, Switzerland. This article is an open access article distributed under the terms and conditions of the Creative Commons Attribution (CC BY) license (https://creativecommons.org/licenses/by/4.0/).

1. Introduction

Coal remains a primary energy source, and thus, the coal mining industry has become a significant economic driver for some countries, including Mongolia. The economic sustainability of coal mining in these countries is largely due to the high profitability and ease of managing surface coal deposits. Surface mining, which includes open-pit mining, mountaintop removal, and dredging, is favored for its lower risk and high productivity. Open-pit mining, in particular, is widely used for large-scale coal extraction. However, this method often leads to severe environmental consequences, such as contamination of water and soil [1–3], and poses risks to local communities due to the creation of large mining voids [4] and its involved risks, such as coal fires [5,6].

Aeolian erosion, which often produces the wind-driven movement of coal particles, has emerged as a significant environmental hazard in open-pit coal mining [7,8]. The survey indicates that a considerable amount of mined coal is lost by preparation, handling, transportation and aeolian erosion in surface mines [9], which can contaminate vegetation, local settlements, and water systems. Fine coal particles can travel long distances, posing serious environmental and health risks [10,11]. For instance, South Korea frequently experiences dust storms originating from the Gobi Desert and Inner Mongolia, which may often contain coal particles. These particles can cause long-term respiratory issues in humans, particularly affecting mining workers [12] as well as local residents. For instance, outbreaks of black lung and silicosis, both respiratory diseases caused by the accumulation of coal dust particles in the lungs, have been reported [13].

In the Gobi Desert, extensive surface coal mining provides crucial economic benefits to Mongolia and supplies energy and coking coal to neighboring countries. However, these mines are highly susceptible to aeolian erosion due to strong winds and low soil moisture, which favor dust storm formation. Observations indicate that between March and June, 50 to 60 days of strong winds (>6.5 m/s) account for 71.9% of the annual dust events in the Gobi Desert. This far surpasses the secondary, weaker dust peak from September to November, which only contributes 6.6% [14]. Another study, based on long-term weather modeling, also found that the Gobi's dust activity is driven by persistent strong westerly winds during the March to June period, coupled with low soil moisture and sparse vegetation [15]. Simple mitigation measures, such as water spraying, are impractical in the Gobi Desert due to the region's scarce water resources. Consequently, significant dust generation, including coal particles, is inevitable. Monitoring and investigating aeolian erosion in these areas is challenging due to the lack of effective sensing methods.

We recognized the need for improved erosion monitoring and, therefore, adopted Sentinel-1 Interferometric Synthetic Aperture Radar (InSAR) time-series analysis to track aeolian erosion processes [16,17], particularly at the large outcrop coal deposits of Ail Bayan and another southern Mongolian coal mine, Tavan Tolgoi. In addition, the study combined InSAR measurements with particle trajectory analysis to monitor erosion pathways. The results from InSAR measurements were validated by multi-band optical image interpretations, particularly focusing on coal dust cover. In the end, we attempted to quantitatively observe coal mine erosion and use it to trace the footprint of coal dust transport on the surrounding terrain.

The study is structured as follows: Section 2 introduces the characteristics of the target area and the datasets used. Section 3 details the methodology. Section 4 presents the outputs from InSAR time series analyses, which are further interpreted in Section 5.

2. Test Site and Data Sets

2.1. Test Area and Its Background

The mining industry, especially for coal, copper, and gold, is a major driver of Mongolia's economy [18,19]. While there has been a shift towards copper production, coal mining remains a vital national resource [19]. This is largely due to Mongolia's estimated 10.2 billion tons of coal reserves [20], which are predominantly found in easily accessible surface open-pit deposits. As shown in Figure 1a, coal deposits are widely distributed across Mongolia, with the southern Gobi Desert area being particularly significant. This region's deposits are more easily mined and transported to China, which is Mongolia's primary coal consumer, importing 82% of its coal [21] as shown in Figure 1b. The sevenfold expansion of coal mining in the last 40 years [22] has been a major driver of Mongolia's recent economic growth, providing national income, employment, and energy [23,24].

Our primary study site is the privately-owned Ail Bayan coal mine in Dornogovi (43.717N, 108.946E), likely developed in the 2010s. Detailed information about this mine is limited. However, the surrounding environment of Ail Bayan presents challenges due to a lack of water resources, transportation networks, and local settlements to support mining operations.

The Tavan Tolgoi coal mine (43.625N, 105.474E) serves as a comparison site. Developed in 2011, it has become one of the world's largest open-pit coal mines, benefiting from superior infrastructure, including water supply systems, a power plant, and a support town. In 2021, Tavan Tolgoi produced 4.48 million tons of coal [25]. Figure 1b,c illustrate the different topographic and hydrological conditions of the two coal mines. Tavan Tolgoi is situated on a rolling plain with ample hydrological resources connected to nearby rivers and underground waters. In contrast, Ail Bayan is located in a small basin without any hydrological network, leading to significantly different operational environments.

We conducted a field survey at these two coal mines in March 2019. The images taken during the field survey highlighted the differences in dust generation between the two coal mines (Figure 1d,e).

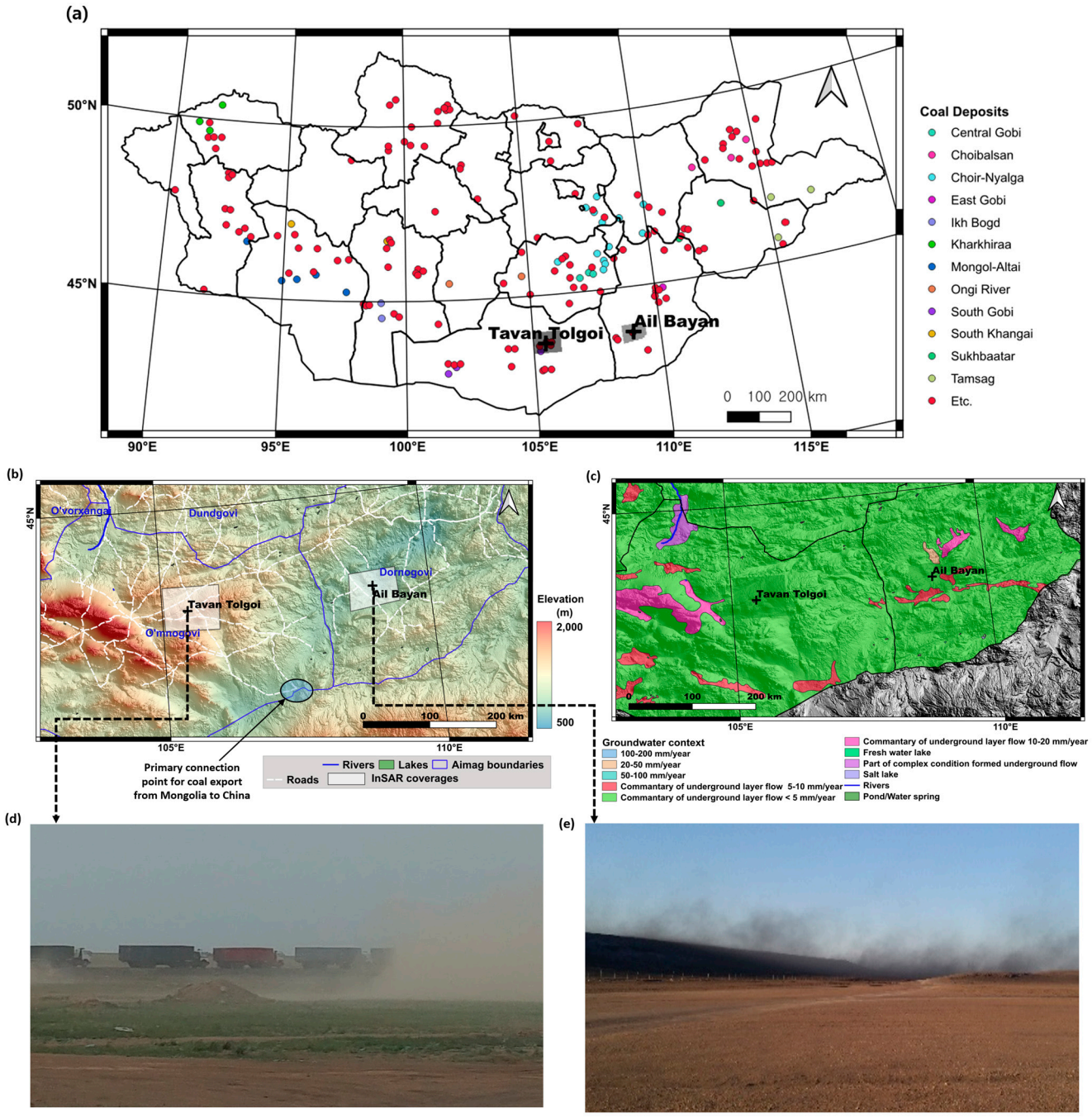


Figure 1. (**a**) Location of study areas, (**b**) geographical and topographic context of Ail Bayan and Tavan Tolgoi coal mines, (**c**) surrounding hydrological contexts (source: https://eic.mn/, accessed on 1 July 2024), (**d**) coal production and transportation at Tavan Tolgoi (43.625N, 105.474E) and (**e**) coal dust generation at Ail Bayan (43.717N, 108.946E) (images were taken in March 2019). Note that the transportation vehicles in Tavan Tolgoi are well-confined so as not to produce coal dust.

2.2. Data Sets

We utilized the European Space Agency (ESA) C-band (wavelength 5.54 cm) Sentinel-1 A/B (hereafter named Sentinel-1) Synthetic Aperture Radar (SAR) imagery, which was ultimately processed into InSAR products. Sentinel-1 provides 5 × 20-m resolution images in the Interferometric Wide Swath (IW) mode, which served as the primary product for this research [26]. We exclusively used the VV polarization mode among the two available modes (VH and VV) on Sentinel-1 [27]. Detailed imaging conditions for the Sentinel-1

images used in this study are presented in Tables 1 and 2. With a 12-day revisit cycle, our dataset comprised 150 ascending and 40 descending InSAR pairs over Ail Bayan, and 300 ascending and 60 descending InSAR pairs over Tavan Tolgoi. The data processing pipeline from ESA's Sentinel Application Platform (SNAP), supplemented with an in-house wrapper [28], was employed to preprocess the InSAR products to a 30-m resolution.

Table 1. Characteristics of employed Sentinel-1 images over Ail Bayan.

	Ascending Mode	**Descending Mode**
Number of Images	139	27
Master image	25 December 2017	10 January 2018
Time coverage	23 January 2017–9 May 2022	24 September 2017–14 August 2018
Heading angle (deg)	−14.0	194.05
Incidence angle (deg)	39.4	37.5
Acquisition time (UT)	10:39	22:51

Table 2. Characteristics of employed Sentinel-1 images over Tavan Tolgoi.

	Ascending Mode	**Descending Mode (Path 62)**	**Descending Mode (Path 135)**
Number of images	154	17	12
Master image	2 November 2019	14 February 2018	22 October 2017
Time coverage	4 January 2017–26 May 2022	11 September 2017–10 March 2018	16 September 2017–19 February 2018
Heading angle (deg)	−14.0	193.94	193.95
Incidence angle (deg)	39.2	39.213	34.14
Acquisition time (UT)	10:47	23:01	23:09

Accurate processing of SAR/InSAR signals necessitates the use of the most recent Digital Elevation Model (DEM) data to reduce DEM errors induced by mining activities. In this study, we utilized the Copernicus 30 m DEM, which was derived from the WorldDEM [29]. The WorldDEM was generated through the InSAR capabilities of the TanDEM-X Mission [30] taken between 2010 and 2014. The German Space Agency (DLR) further processed the WorldDEM to create the Copernicus DEM, enhancing its quality through operations like gap filling, flattening of water bodies, and coastline adjustment, resulting in a superior representation of recent topography [31].

To validate our InSAR results using multispectral signatures, we employed multiple Sentinel-2 images acquired between 2018 and 2019. We used Level-2A images, which contain orthorectified Bottom-Of-Atmosphere (BOA) surface reflectance data, from the Copernicus data hub (https://scihub.copernicus.eu/, accessed on 1 July 2024) covering the 2018 period.

For particle trajectory analyses associated with the InSAR tasks, we utilized weather datasets from the Global Data Assimilation System (GDAS) [32]. We also produced quarter-degree resolution wind datasets using the European Centre for Medium-Range Weather Forecasts reanalysis V5 (ERA-5) land data [33], processed through Google Earth Engine (GEE).

3. Methods

The processing algorithms utilized in this study can be summarized as follows: (1) InSAR processing to detect topographic migration; (2) optical data processing to conduct further interpretation together with InSAR data; (3) trajectory analyses to track the behavior of blown particles.

3.1. InSAR Time Series Analyses and Decomposition

The primary technical basis of our approach is establishing a time series for coal mine erosion monitoring using InSAR. However, this task is complicated by the decorrelation of InSAR signatures on continuously changing topographies. As a result, we were unable to use Permanent Scatterer Interferometry (PSI) analyses [34,35] due to decorrelation issues arising from rapid topographical changes and the lack of permanent scatterers (PS). This means that only rocky surfaces among natural landscapes produce the proper PS [36]; thus, sandy surfaces and steppe, like our target area, are not preferred for PSI observation. It is also important to note that PSI algorithms retrieve the time-series phase of PS from a single master stack [37]. Therefore, PSI is more fragile for long-term monitoring of extensively varying surfaces, such as coal mine pits.

To address these issues, we opted to use a variant of the Small Baseline Subset (SBAS) technique [38], which is better suited for tracing regional deformation, as shown in [39–41]. Specifically, we employed the Miami InSAR Time-series software (MintPy) (v. 1.1.2.) [42], an improved version of SBAS. MintPy offers significant advantages for our case, which requires high-density scatterers with greater reliability to trace erosional topography primarily on coal deposits. MintPy enhances SBAS in the following ways:

- Atmospheric and topographic noise removal: MintPy uses external atmospheric data or a topography-dependent approach to eliminate atmospheric phase screen (APS) together with dereamping and topographic noise removal algorithms.
- Phase unwrapping error correction: MintPy incorporates methods to correct or exclude phase unwrapping errors, ensuring more reliable output.
- Improved phase inversion approach: MintPy provides an enhanced phase inversion approach, resulting in more accurate measurements.

These improvements make MintPy particularly suitable for our study, allowing us to achieve the high-density scatterers necessary for detailed erosion monitoring in coal mining areas. Moreover, we constructed SBAS connections employing short spatial (<150 m) and temporal (<25 days) baselines, as shown in Figure 2. These thresholding criteria, combined with the low vegetation in the target area, causing less decorrelation, resulted in high spatial correlations (>0.7) for all InSAR pairs and consequently contributed to achieving high-density scatterers.

In particular, MintPy's inversion approach, described in [42], is as follows.

A system of M linear observation equations with the phase time-series $\phi = [\phi_2, \ldots, \phi_N]^T$ as the vector of the $N-1$ unknown parameters can be expressed as follows, assuming a base acquisition at time t_1:

$$\Delta\phi = A\phi + \Delta\phi_e \quad (1)$$

where $\Delta\phi = [\Delta\phi_1, \ldots, \Delta\phi_M]^T$ is the phase vector, $\Delta\phi_j$ is the phase of the j^{th} interferogram, A is an $M \times (N-1)$ design matrix representing the InSAR acquisition pairs and $\Delta\phi_e$ is the residual phase vector.

Equation (1) can be solved by minimizing the *L2*-norm of $\Delta\phi_e$ as follows.

$$\underline{\varphi}\text{argmin} \; ||W^{1/2}(\Delta\phi - A\phi)||_2 = (A^T W A)^{-1} A^T W \Delta\phi \quad (2)$$

where $\underline{\varphi}$ is the estimated raw phase time-series and W is an $M \times M$ diagonal weight matrix. According to [42], the weight matrix can be constructed in one of the following ways: (1) an identity matrix, as used in conventional SBAS techniques; (2) spatial coherence at each pixel [43]; (3) the inverse of the phase variance [44]; (4) a nonparametric Fisher information matrix that accounts for information loss due to noise and decorrelation [45].

In this study, we employed a spatial coherence-based weighting matrix and APS construction based on the Generic Atmospheric Correction Online Service (GACOS) [46]. We also used a loop closure phase (LCP) to filter off the erroneous InSAR time series point.

Assuming three unwrapped interferograms in three InSAR pairs in time series 1, 2, and 3, its LCP is as follows [47]:

$$\Delta_{123} = \varphi_{12} + \varphi_{23} - \varphi_{13} \quad (3)$$

where Δ_{123} is the LCP in time series phase angles of 1, 2 and 3 images, φ_{12} is the difference of phase angles of the 1–2 pair, and so on.

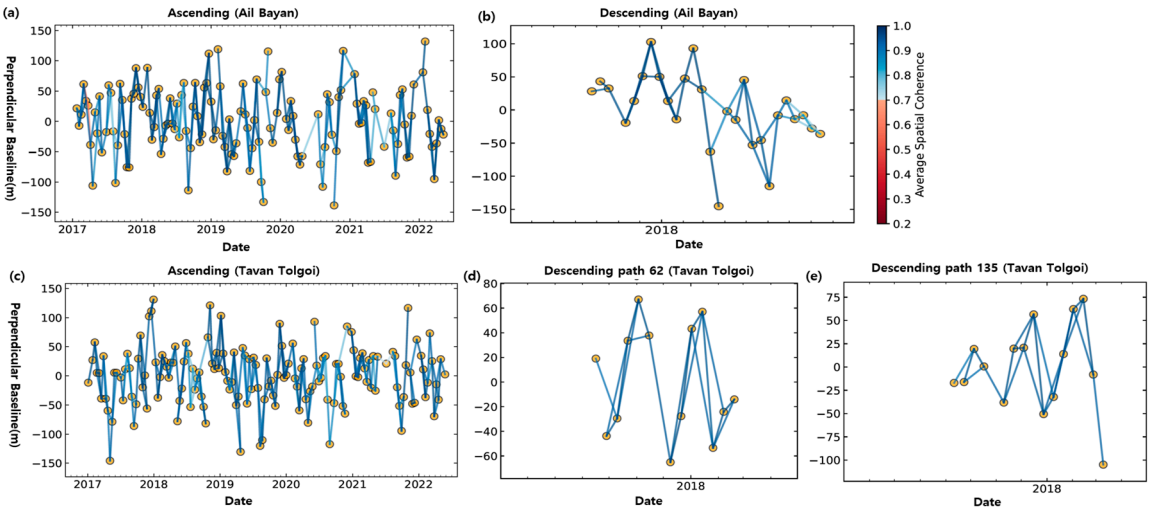


Figure 2. Acquisition times and connection graphs of employed ascending/descending Sentinel-1 InSAR pairs over Ail Bayan (**a**,**b**) and Tavan Tolgoi (**c**–**e**). Note that the phase coherences of InSAR pairs are always higher than 0.7. In Ail Bayan, the ascending mode InSAR observations were interpolated into the descending mode time domain for decomposition. Similarly, over Tavan Tolgoi, the ascending and descending mode observations in path 62 were interpolated into the descending mode time domain of path 135. While the thresholds for perpendicular and temporal baselines were set to 150 m and 25 days, respectively, some InSAR pairs exceeding these thresholds were included to enhance interferometric coverage.

If the interferogram is free of errors such as unwrapping failures, ionospheric disturbances, and orbital artifacts, the LCP should be zero [48]. However, residual errors can still occur due to surface conditions that cannot be fully compensated for, such as soil moisture variations [47]. Therefore, the LCP can be used to identify outliers in phase angle [49,50] within the target area where soil moisture is expected to be low [51]. Considering that we are working with InSAR time series over a constantly moving surface, LCP-based error reduction is an effective method for obtaining reliable phase vectors.

Implementing error regulation techniques and the inversion procedure of MintPy produced a high-density time series observation, even after filtering out erroneous InSAR points. Figure 2 presents the connection of InSAR pairs in Ail Bayan and Tavan Tolgoi. It is worth noting that all InSAR pair connections had a high spatial coherence due to minimal interference from vegetation and rainfall [52], an advantage of InSAR processing in an environment such as the target area.

The technical details for generating the InSAR pairs for delivery to MintPy are as follows. First, SAR images and corresponding connections suitable for SBAS analysis were selected from the Alaska SAR Facility (ASF) online search tool (https://search.asf.alaska.edu, accessed on 1 July 2024). In particular, the ESA SNAP version 10.0.0 software, which utilizes the Graph Processing Toolbox (GTP), was employed to generate the InSAR pairs. An in-house Python wrapper streamlined this process to generate phase angle and coherence images. These outputs were subsequently processed by Statistical Cost, Network Flow Algorithm for Phase Unwrapping (SNAPHU) [53], a two-dimensional phase unwrapping tool. The unwrapped phase and coherence images were then georeferenced and formatted for compatibility with the MintPy software.

Upon the ascending/descending LOS products, the vector decomposition was conducted according to the method described, as follows [54]:

$$disp_{los} = \left| -sin\theta cos\alpha \quad sin\theta sin\alpha \quad cos\theta \right| \begin{vmatrix} disp_{EW} \\ disp_{NS} \\ disp_{UD} \end{vmatrix} \tag{4}$$

where $disp_{los}$ is the line of sight (LOS) displacement, ($disp_{EW}$, $disp_{NS}$, $disp_{UD}$) are the (*East-west*, *North-south*, *Up-down*) axis displacements and θ, α are the heading and incidence angles, respectively.

To effectively decompose the deformation time series, we must address two key challenges: (1) synchronizing the ascending and descending observations in time, and (2) smoothing the deformation data to minimize noise and prevent artifacts in the resulting velocity components. To tackle this, we applied spatiotemporal spline interpolation, which enables us to estimate the ascending deformation values at the exact times of the descending observations, aligning the datasets in the time domain. By fitting a smooth spline curve, we also reduce noise and avoid abrupt changes in deformation velocity, resulting in more reliable and interpretable decomposed velocity components [55].

As the heading angles of the satellite can be approximated to 0° and 180°, the contribution of East-West displacement to horizontal displacement is far more significant, about three times in Sentinel-1 image acquisition geometry than that of North–South displacement. Therefore, horizontal displacement extracted by decomposition can be better constrained by omitting North-South, as follows:

$$disp_{los} = \left| -sin\theta cos\alpha \quad cos\theta \right| \begin{vmatrix} disp_{H} \\ disp_{V} \end{vmatrix} \tag{5}$$

where $disp_H$ is the horizontal directional displacement, $disp_V$ is the vertical directional displacement. In this study, the Tavan Tolgoi area has three InSAR coverages, as shown in Table 2. Although it is possible to solve them for 3D decomposition, i.e., North-South, East-West, and Up-Down directions, heading and incidence angle differences in two descending modes, as presented in Table 2, are tiny. Thus, it is better to decompose vertical/horizontal components using an overdetermined linear system, as expressed in (5). Overall, InSAR processors and involved data flows were demonstrated in Figure 3.

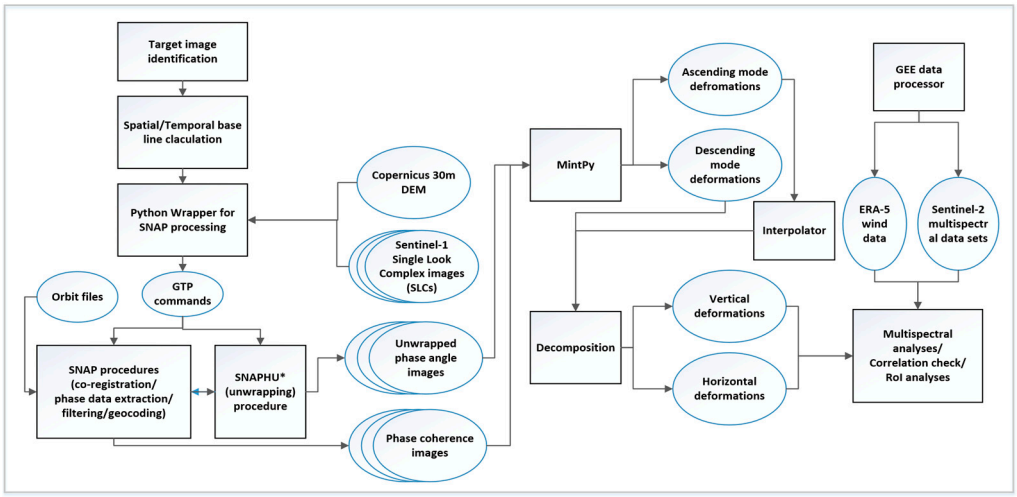


Figure 3. Processing workflow for InSAR time series data, including integration with other satellite and spatial datasets.

3.2. Processing of Optical Images

We utilized Sentinel-2 multispectral images to interpret InSAR outcomes further. We extracted the spectral signature of significant sample areas and applied the spectral information divergence (*SID*) [56], which measures the divergence between the spectral signatures of the samples and target areas by calculating the relative entropy of their respective probability distributions. The sampling areas of spectral signatures were decided by the outcomes of InSAR, as described in the following sections.

To track soil moisture in the target areas, the resolution of spaceborne soil moisture products, typically around 0.25 degrees [57], is insufficient. Consequently, we introduced an alternative spectral index of Sentinel-2, the Normalized Multi-band Drought Index (NMDI), defined as follows [58]:

$$NMDI = (R_{860nm} - (R_{1640nm} - R_{2130nm}))/(R_{860nm} + (R_{1640nm} - R_{2130nm})) \quad (6)$$

where R_{860nm}, R_{860nm} and R_{2130nm} are the apparent reflectances observed by the satellite sensor in the 860 nm (band 8 of Sentinel-2), 1640 nm (band 11) and 2130 nm (band 12) wavelengths. NMDI values typically range from -1 to 1, with higher values indicating less soil moisture under the condition of low vegetation (e.g., Leaf area index (LAI) < 1.0) [58,59], which is applicable in our study area

3.3. Trajectory Analyses

To interpret InSAR data in comparison to particle trajectories of aeolian processes, we conducted multiple simulations of blown particles using the Hybrid Single-Particle Lagrangian Integrated Trajectory (HYSPLIT) model [60,61]. These simulations were synchronized with the InSAR observations period. For efficient execution, we implemented a Python wrapper to manage multiple simulations, utilizing the Python interface for HYSPLIT, known as pySPLIT [62]. The pySPLIT implementation automatically downloaded GDAS weather data at a 1-degree resolution from the National Center for Environmental Prediction (NCEP, https://www.nco.ncep.noaa.gov/pmb/products/gfs/#GDAS, accessed on 1 July 2024) for the specified period. These data were then used in the HYSPLIT model executions for every hour during the period. The resulting trajectory outputs were summarized and converted into geotiff raster data, allowing for a detailed inter-comparison with the InSAR time series data.

4. Result

The Sentinel-1 InSAR time series datasets for the Ail Bayan area were processed as described and their outputs are illustrated in Figures 4 and 5. The deformation patterns caused by coal production, indicated by substantially negative LOS velocity, are clearly visible in the coal mining areas, as shown in Figure 4c,d. In addition, the footprints of aeolian interactions, including both erosion and deposition, observed in the ascending mode (mostly positive LOS velocity), are well presented in Figure 4c. Similar deformation patterns are evident in the descending mode (Figure 4d).

The decomposed horizontal deformation, shown in Figure 5a, reveals a clear deposition area on the eastern side of the coal mine, which aligns with the average wind direction, prevailing westerly wind, derived from ERA-5 data processed using GEE. This horizontal deformation mainly corresponds with the positive vertical deformation shown in Figure 5b. Significant aeolian erosion is also seen as vertical cuts, indicated by negative deformation, in Figure 5b.

The InSAR time series results for Tavan Tolgoi, shown in Figure 6, reveal highly distinctive and confined erosion and deposition patterns around the coal mining and processing areas. The decomposition results in Figure 7 indicate that significant erosion and deposition are concentrated solely around the coal mine areas, suggesting that aeolian erosion and deposition are not widespread in the region.

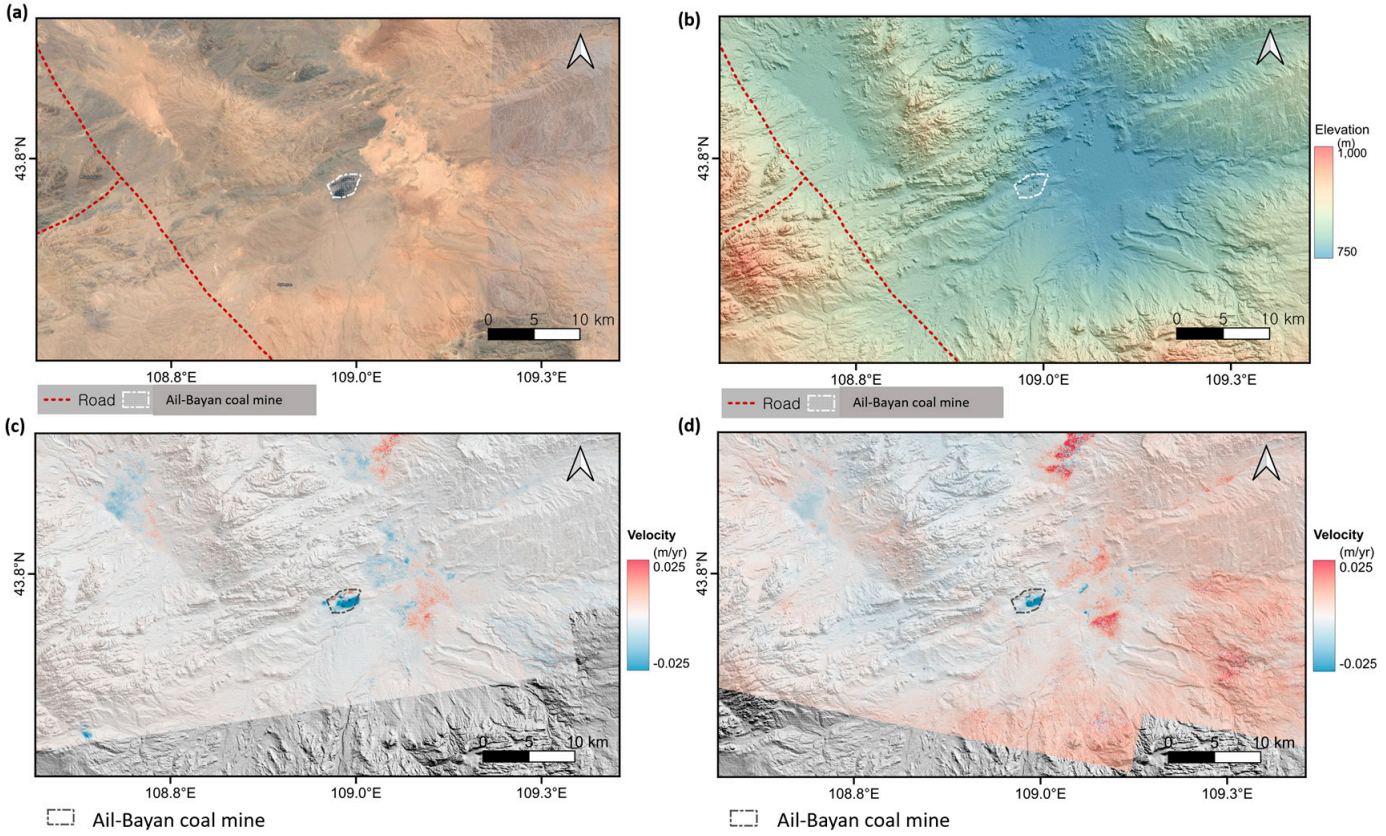


Figure 4. (**a**) Google map, which reveals the details of Ail Bayan, (**b**) topography presented in Copernicus 30 m DEM, (**c**) ascending LOS velocity and (**d**) descending LOS deformation velocity.

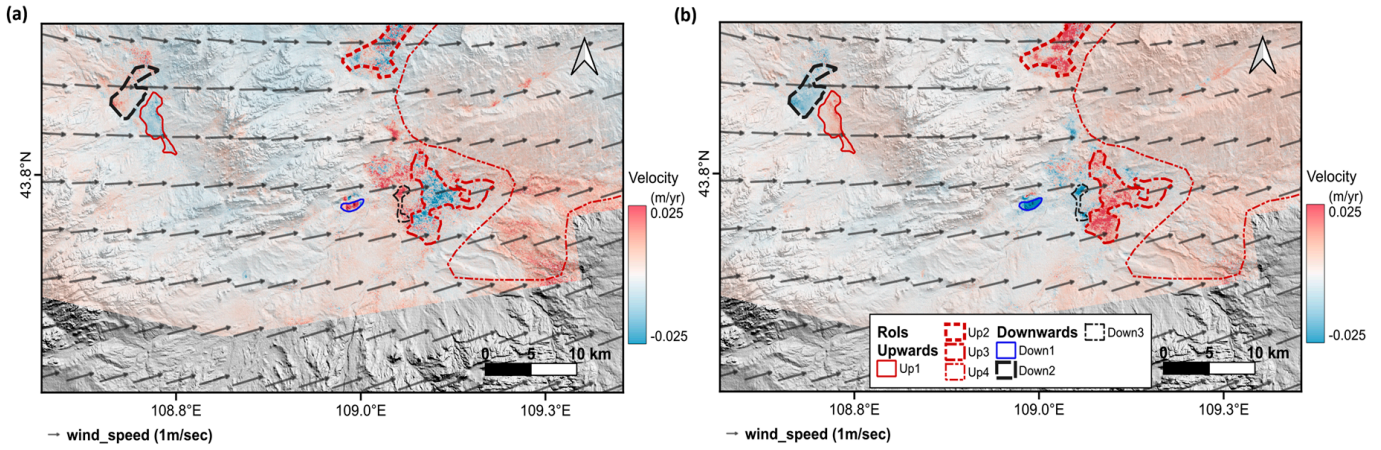


Figure 5. (**a**) Decomposed horizontal velocity and (**b**) vertical velocity in Ail Bayan. The overlaid average wind velocities were extracted using GEE and interpolated to a 1 km resolution from the original 11.132 km ERA5-Land data using kriging.

Further interpretation of the data, in conjunction with trajectory simulations and optical data processing, as described in the following section, provided quantitative insights into the environmental impacts of coal mining activities. This integrated approach allowed for a more comprehensive understanding of the extent and nature of the environmental changes caused by coal mining activities.

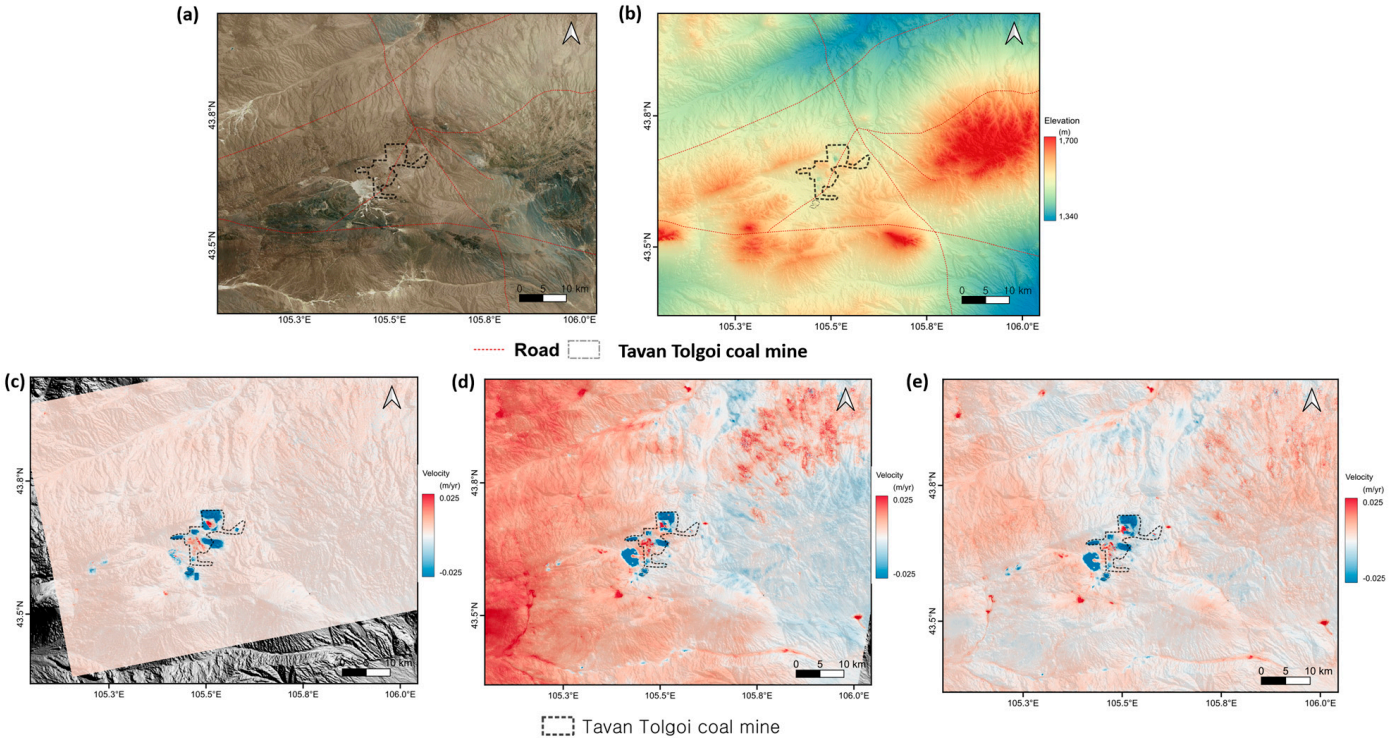


Figure 6. (**a**) Google map which reveals the details of Tavan Tolgoi, (**b**) topography presented in Copernicus 30 m DEM, (**c**) ascending LOS velocity, (**d**) descending LOS deformation velocity of path 135 coverage, and (**e**) descending LOS deformation velocity of path 62 coverage.

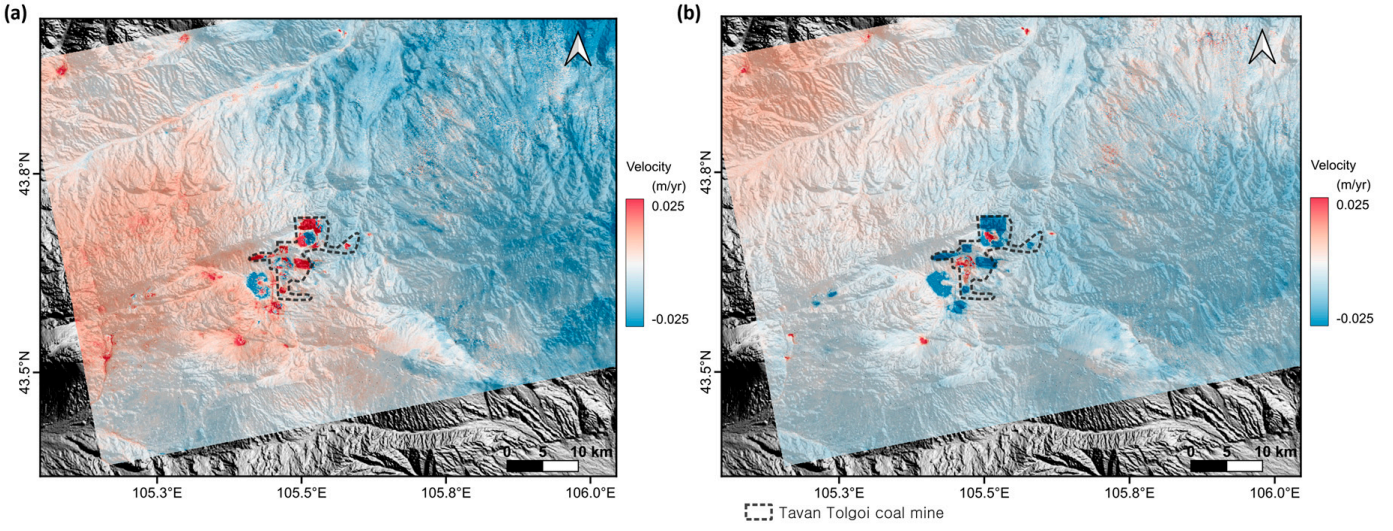


Figure 7. Decomposed velocities in Tavan Tolgoi: (**a**) horizontal velocity and (**b**) vertical velocity. Note that the wind directions are similar to those in the Ail Bayan area, blowing from west to east.

5. Interpretation & Validation

From the vertical decomposition results of the Ail Bayan area presented in Figure 5b, we identified seven regions of interest (RoIs): four upslope areas (Up1–Up4) and three downslope areas (Down1–Down3). The basis for defining the Regions of Interest (RoIs) is as follows: (1) Down1 corresponds to the major mining area; (2) Down2 appears as an erosional area, though the driving factor remains unclear; (3) Down3 is a distinguished erosion zone surrounding the major mining area, likely caused by windblown transport; (4) Up1 is connected to Down2 and exhibits weak deposition; (5) Up2 is an apparent

and independent aeolian deposit; (6) Up3 is the most predominant aeolian deposit, likely serving as the primary site of coal dust accumulation through aeolian processes; (7) Up4 is a large background area potentially affected by coal dust and requires further investigation.

Based on ascending and descending satellite data, the deformation patterns in Figures 4 and 6 clearly differentiate the effects of coal mining and aeolian erosion. Coal mining induces vertical subsidence due to the extraction of surface seams, resulting in negative LOS displacements in both acquisition modes, with the most significant impact in active mining zones like Down1. In contrast, aeolian erosion, driven by wind-induced particle movement, causes both horizontal and vertical displacements that are more subtle and widespread [63,64]. InSAR data thus reveal distinct deformation signatures of concentrated subsidence from mining and more diffuse, gradual changes from aeolian interaction.

For the InSAR ascending, descending, horizontal, and vertical time series, deformation velocities in RoIs were extracted and compared with ERA-5 mean wind velocities, as shown in Figure 8. Down3 deformation clearly follows wind speed patterns, especially in ascending mode as shown in Figure 8a. This pattern is also observed in the other three observation modes but not as clearly as in the ascending mode case. This is because ascending mode observations encompass a longer timeframe, thus revealing clearer yearly periodic patterns. The other RoIs did not show a clear correlation with wind velocity. For instance, the migration pattern in Down1 is likely related to coal production rather than wind velocity.

To clarify the relationship between deformation and wind patterns, we created correlation maps between the deformation time series at each pixel and average wind speeds, as shown in Figure 8. These maps highlight areas where surface deformations are under the influence of temporal wind strength. Figure 9a shows the long-term trend of wind influence on surface deformation in InSAR ascending mode. Except for Down1 and Down2, surface deformations in all RoIs generally followed wind velocity patterns over a five-year period, suggesting aeolian erosion. The correlation maps of descending, vertical and horizontal velocity in Figure 9b–d, corresponding to short-term deformation, showed a similar pattern, although there are some deformations that were not affected by the temporal wind velocity pattern, such as the central part of Up3. Those maps also showed some wind-related migrations in the southeastern part of Up4.

We employed the SID spectral matching algorithm to examine the spectral responses of all test areas and attempted to interpret them in the context of regional deformation. We first obtained the average spectral signatures of Down3/Up3 and Down1 from the Sentinel-2 image (see Figure 10e,f), and then applied the spectral matching algorithm to the signatures of the entire image. The average spectral signature of Down1 is representative of the spectrum of a coal particle, while the average spectral signature of Up3 is likely to represent that of a different wind-blown mineral, referred to as fine mineral particles (FMPs), as observed in the visual band image and deformation velocity map. The results of the analyses are shown in Figure 10. Figure 10a–d show the extent of coal particles and other mineral deposits from early spring to summer 2018. Coal particles are centered around the mine area, and FMP deposits are strongly distributed to the eastern side of the coal mine, with occasional extensions to the south.

Given all analyses, the interpretations of aeolian deformation are as follows.

Up1 can be interpreted as partially weak aeolian deposition along a hillside opposite the wind direction, with only limited involvement of coal dust blown from Ail Bayan. There is a possibility of interaction with blown coal from a private coal mine to the southwest, which is not included in the target area. Up1 is associated with Down2, where surface erosion is occurring. Up2 is another aeolian deposition area that possibly shares a similar origin with Up1. In this area, other aeolian mechanisms that are less likely to be associated with coal mine-blown particles should be considered.

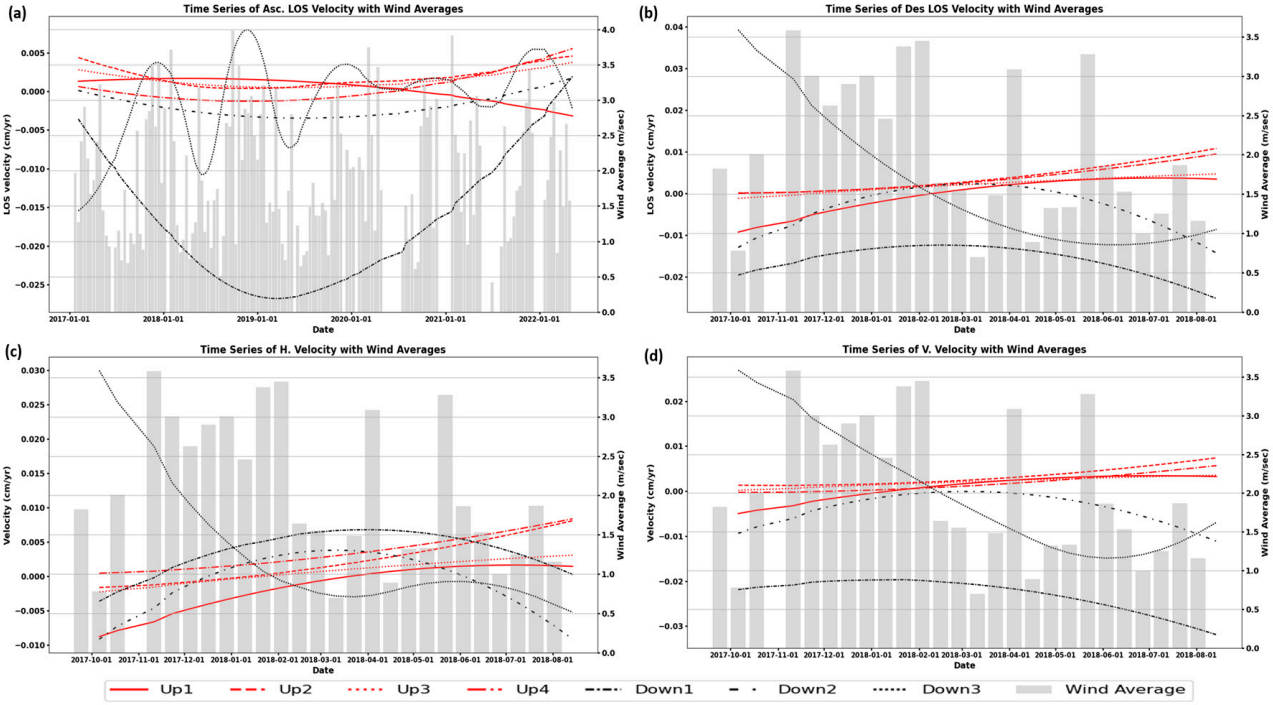


Figure 8. The behavior of seven RoIs along with mean wind velocities in different modes: (**a**) ascending mode, (**b**) descending mode, (**c**) decomposed horizontal deformation velocities, and (**d**) decomposed vertical deformation velocities.

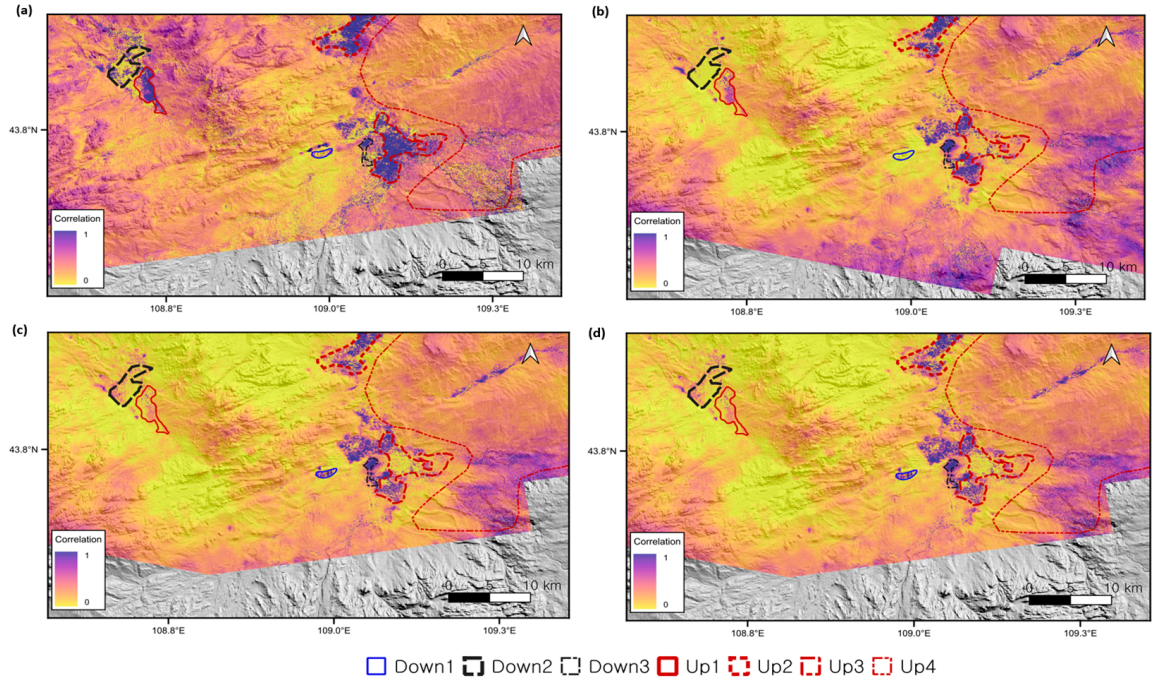


Figure 9. Correlation maps between InSAR deformation velocities and average wind velocities for corresponding periods in (**a**) ascending mode, (**b**) descending mode, (**c**) horizontal component of decomposed InSAR velocities, and (**d**) vertical component of decomposed InSAR velocities.

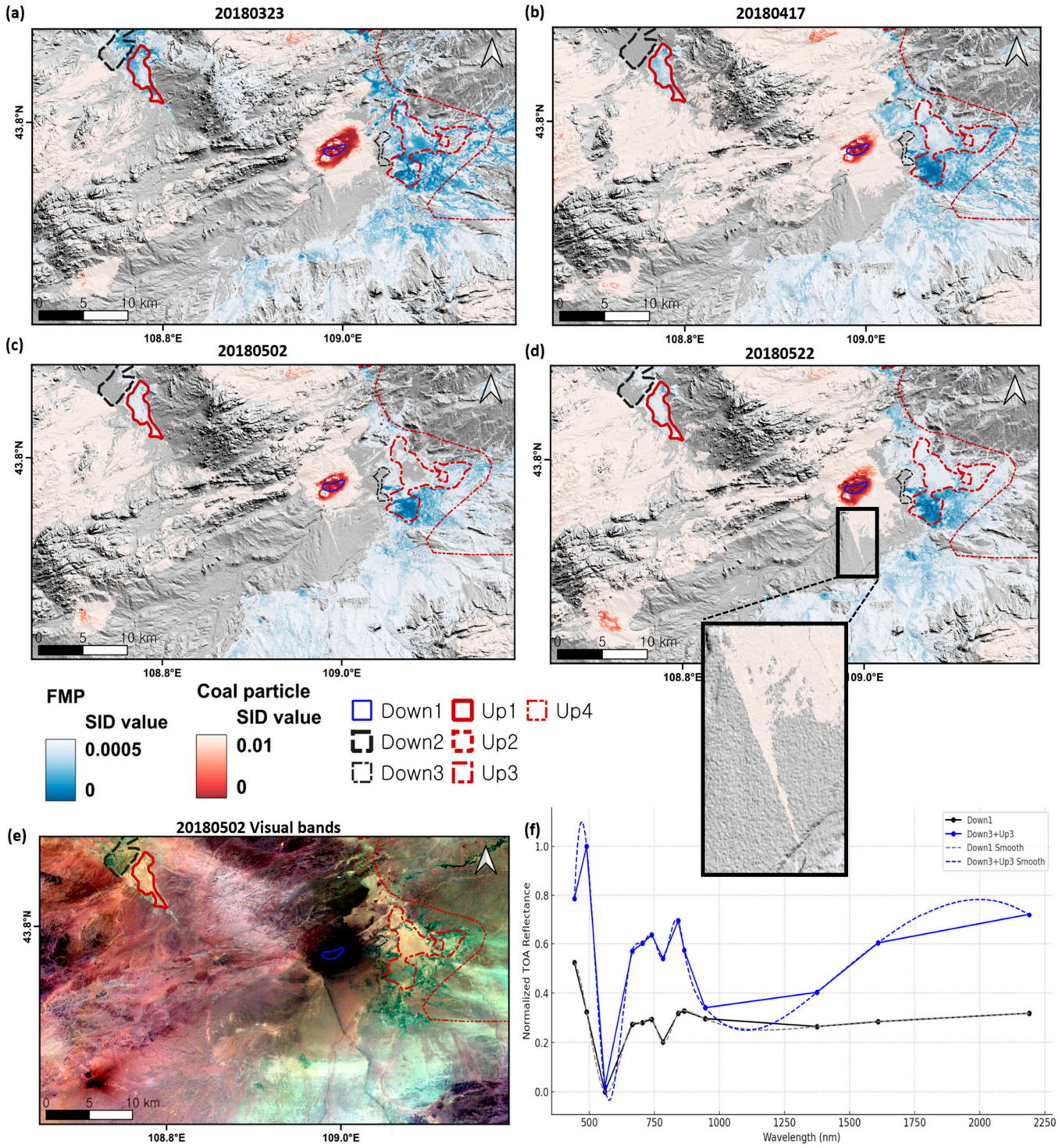


Figure 10. Spectral signature analyses using Sentinel-2 time series images on (**a**) 23 March 2018, (**b**) 17 April 2018, (**c**) 2 May 2018, and (**d**) 22 May 2018. Note that a lower SID value indicates greater spectral similarity. (**e**) Visual band view of Sentinel-2 image (2 May 2018), (**f**) spectral signatures in Down1 and Down3/Up3 areas representing coal mine and major FMP aeolian sites.

Down1 represents the mining part of the coal mine. Coal particles in Down1 have spread due to coal production and transport activities, filling areas with a coal particle SID of less than 0.005, as shown in Figure 10. Evidence of this particle spread can be seen in the long trail along the transport road highlighted in the zoomed-in view of Figure 10d. Notably, the velocity trend in Down1 increased from 2019 to 2022 (see Figure 8a), which

may be related to the economic downturn during the COVID-19 pandemic, when reduced consumption led to the accumulation of coal piles. The dispersed coal particles from Down1 caused horizontal and vertical deformations of several centimeters, as seen in the InSAR observations, and their extent can be inferred from the areas where the coal particle SID is less than 0.01, as shown in Figure 10. It is worth noting that these wind-blown coal particles spread from southwest to northeast, consistent with the annual mean wind direction at an altitude of 10 m.

A major aeolian site is located in the area encompassing Down3 and Up3. The spectral signatures in this region do not resemble major coal compounds, but optical images and ground observations suggest that they are composed of fine particles likely rich in silicate, sulfur, and other minerals, i.e., FMPs [12,13].

The coal particles around Down 1 are generally not directly subject to saltation, the main aeolian erosion mechanism, as estimated by the fact that 70% of the coal particles are larger than 3 mm [65]. The particle size driven by saltation must be between 0.007 and 0.7 mm [66], so only coal particles that have been further degraded during production and transport can be blown away by saltation or partially transported by creeping and distributed, as shown in Figure 10. On the other hand, FMPs from coal piles are much smaller in diameter [13] and are, therefore, directly subjected to saltation and blown away. Due to this difference in particle size, the critical wind speeds acting on the FMPs are different from those of the coal particles and show a distinct directional distribution with seasonal wind changes, as shown in Figure 11a. In autumn to winter, when the northwesterly winds are strong enough, FMPs are blown from the Down3 region (see the wind speed dependence in Figure 8b) and accumulate in Up3. It is worth noting that the wind speed and direction extracted from the ERA-5 wind data at 10 m altitude are consistent with the direction of FMP deposition.

The ratio of wind velocity at 10 m altitude to friction velocity, which is denoted as $u*$ and interacts with the particle on the ground, is given by the following equation:

$$\frac{W(10)}{u*} = \frac{1}{\kappa}\ln\left(\frac{10}{z_0}\right) \quad (7)$$

where κ is the von Kármán constant (approximately 0.4), z_0 is the aerodynamic roughness length, W (10) is wind velocity at 10 m altitude and $u*$ is friction velocity. Darmenova et al. [66] calculated the horizontal flux by saltation in the Gobi Desert based on Shao's model [67] and Marticorena and Bergametti's model [68], respectively. The outcomes showed that at least 0.3 to 1 m/s friction velocity is required to produce meaningful horizontal particle emission by saltation according to the conditions of the typical Gobi Desert, i.e., approximately 0.001 to 0.08 m in Z_0 and the typical climatic factors of the Gobi Desert (see [66] for more details). Figure 11b shows that the friction velocities in Ail Bayan with various Z_0 can reach that level during fall to winter by a predominantly westerly wind direction. Therefore, we can understand the westward directional aeolian connection between Down3 and Up3.

The southeastern side of Up4 may also be affected by blown coal particles. Since the deposition of particles smaller than 100 nm among FMPs is influenced by Brownian motion [69], we conducted trajectory simulations using PySPLIT to investigate the processes involving the migration of these small particles, as shown in Figure 11c,d. These simulations indicate that FMPs produced from the mining area by Brownian motion pass through the less active aeolian areas identified in the correlation maps, such as Down2, Up1, Up2, and Up4, especially during the winter season (Figure 11d). Particles transported at low pressure remain suspended and are unlikely to interact with the terrain by deposition. This is why we focused only on trajectory points with pressures above 900 hPa. The trajectory points appear to correspond to the low coal and mineral component distribution shown in the SID analyses, i.e., coal particle SID around 0.01 or FMP SID around 0.005, in Figure 10.

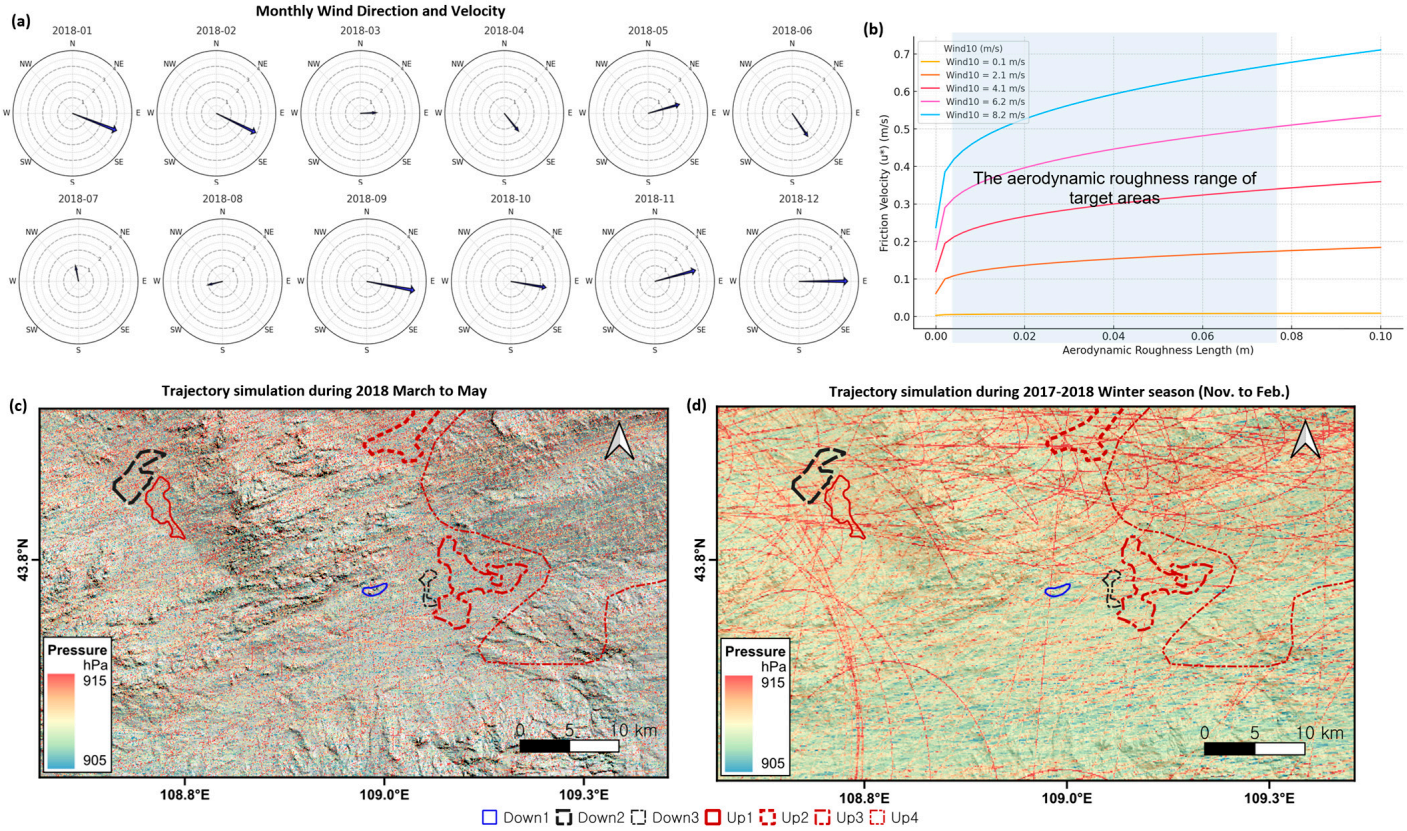


Figure 11. Wind factors influencing coal mine dust generation: (**a**) monthly wind velocity at an altitude of 10 m, (**b**) friction velocities for different 10 m wind velocities and roughness lengths, (**c**) trajectory simulations originating from the coal mine during the sand dust season from March to May 2018, (**d**) trajectory simulations during the summer season of 2018.

Our main concern at this stage is to understand the factors which led to the widespread distribution of coal dust on Ail Bayan, which contrasts with the results from the Tavan Tolgoi coal mine, where the InSAR deformation maps show no evidence of widespread coal dust blowing. We analyzed the soil moisture in the coal mine to determine the cause of the strong aeolian process in Ail Bayan. It is well known that water spraying is the best way to prevent the aeolian erosion of coal piles [70,71]. For example, a 0.7 percent improvement in the moisture content of coal reduces dust by 30–50 percent [72]. As shown in Figure 12a–d, the soil moisture in the Ail Bayan coal mine is half that of the Tavan Tolgoi coal mine. Compared to the well-developed water management facilities at the Tavan Tolgoi Coal Mine, which used 468,595 m^3 already in 2013 [73], the limited water resources at Ail Bayan, shown in Figure 1, suggest that the Ail Bayan Coal Mine cannot rely on water spraying to reduce mine dust, resulting in widespread mine dust generation.

The environmental risks from such coal mine erosion and dust generation can be considered in two forms: a regional factor, which affects neighboring countries, and a local factor, which is confined to the provincial environment. Figure 13 illustrates the potential risks from these two factors. As shown by the HYSPLIT forward trajectories in Figure 13a,b, the dust from the Southern Gobi coal mines spread rapidly and reached most of northeast Asia within two or three days. Springtime sand and dust storms are likely to contain coal mine dust as they carry not only sand dust but also quantities of FMPs that are more harmful to human health.

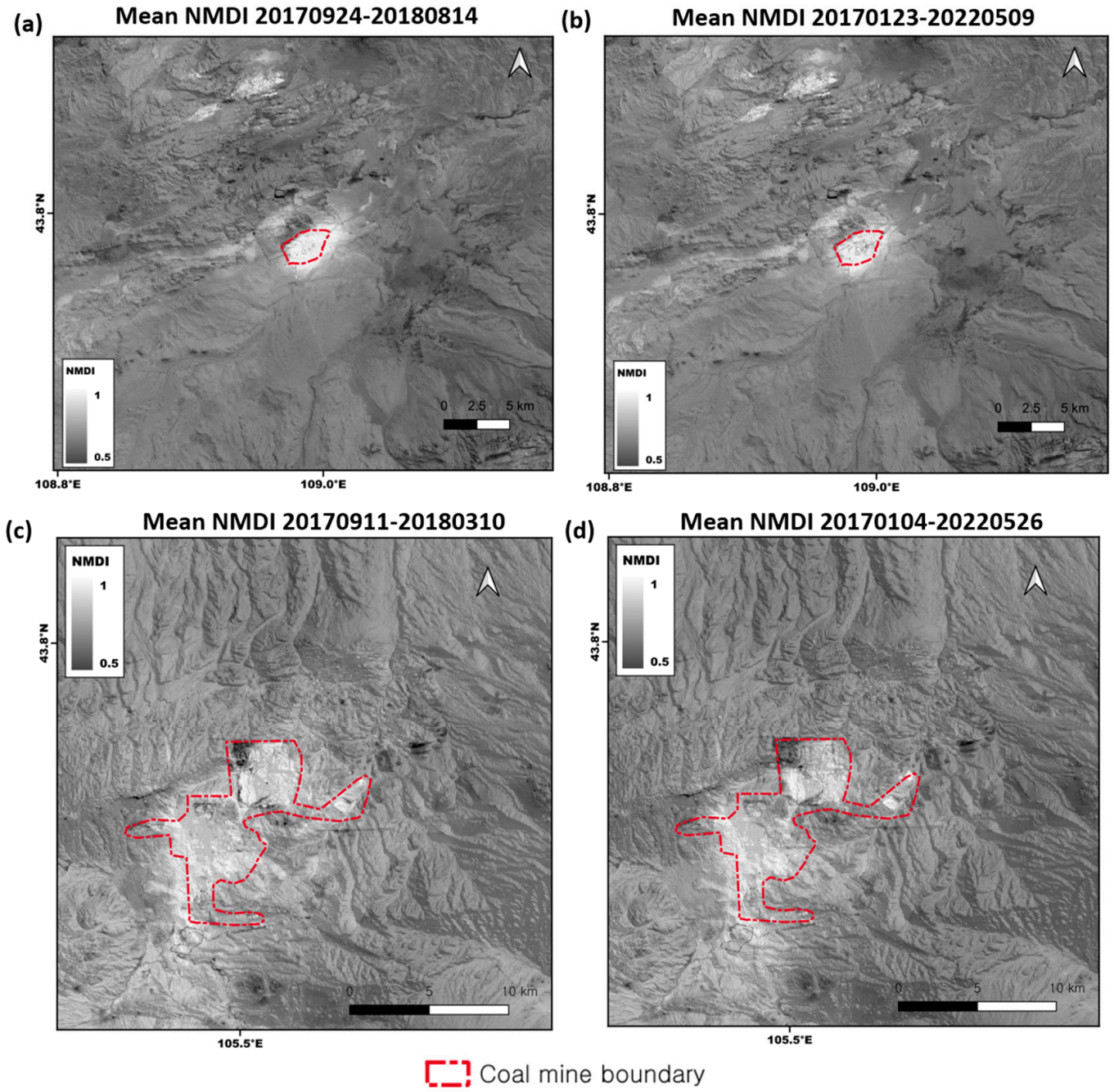


Figure 12. Average NMDI maps for (**a**) Ail Bayan from 24 September 2017 to 14 August 2018, (**b**) the same region from 23 January 2017 to 9 May 2022, (**c**) the Tavan Tolgoi region from 11 September 2017 to 10 March 2018, and (**d**) the same region from 4 January 2017 to 26 May 2022.

On the other side, particles carried by saltation cause enormous damage to the local ecosystem, as can be seen from the FMP-covered soil and vegetation in Figure 13c. In particular, the damage of coal mine dust to vegetation is clearly visible, and this vegetation destruction will make the environment more vulnerable to sand dust events [15].

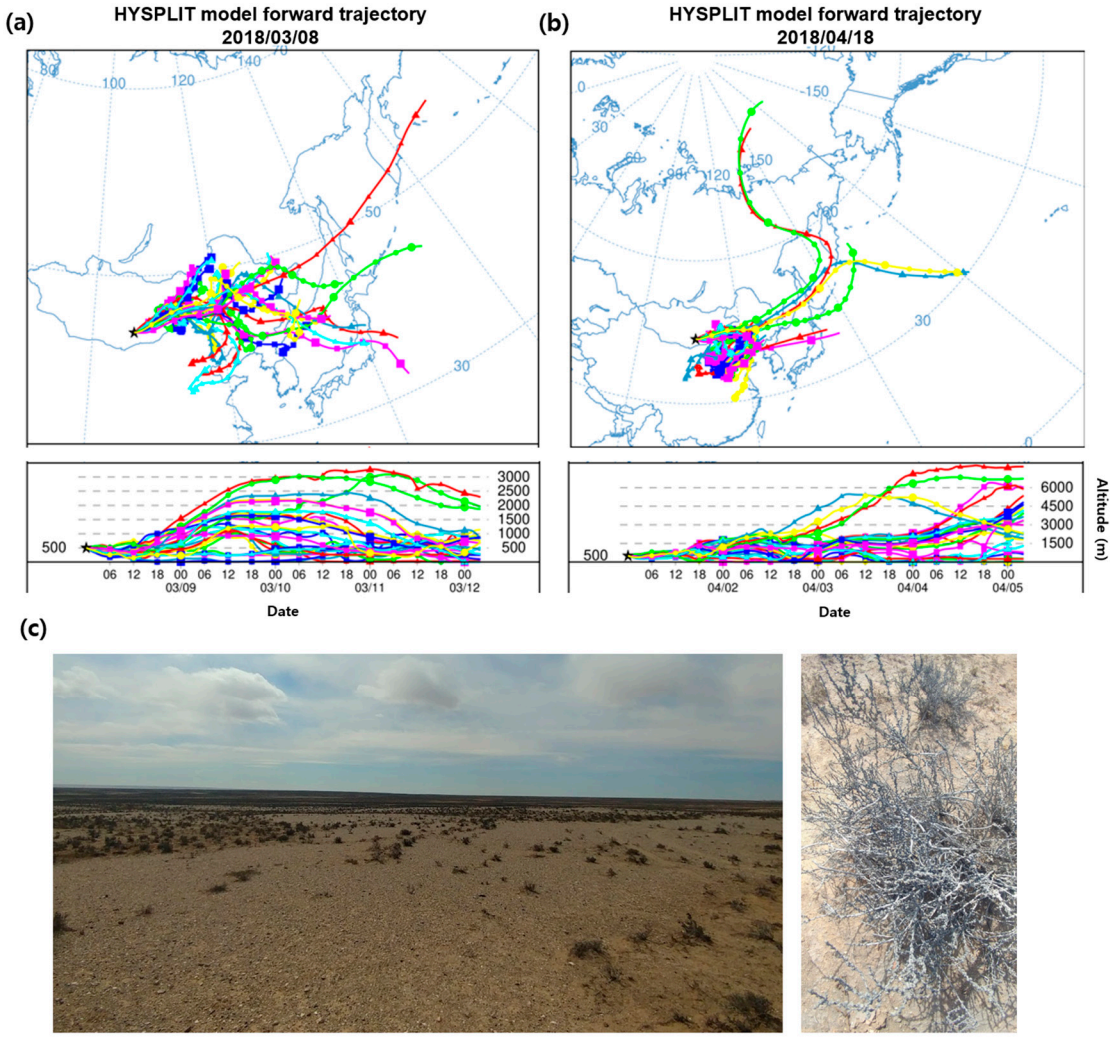


Figure 13. Environmental consequences of coal mine dust generation: (**a**) HYSPLIT trajectory simulations originating from the coal mine in 8 March 2018, (**b**) HYSPLIT trajectory simulations originating from the coal mine in 18 April 2018, using an ensemble HYSPLIT model with 150-h forward trajectory options. (**c**) Ground photos from Down3 area in Ail Bayan showing contaminated soil and vegetation by blown FMP (images were taken in March 2019).

6. Conclusions

This study aimed to establish an InSAR methodology for tracking aeolian processes in coal mines by monitoring land surface deformation in the spatiotemporal domain. Employing Sentinel-1 time series processing, we successfully observed topographic changes caused by aeolian erosion in southern Mongolian coal mines. Although further integration with trajectory simulations and optical data processing was required to detect detailed footprints of blown coal particles, this study demonstrated the potential of InSAR time series in tracking aeolian surface changes and mining activities.

This methodology can be applied to monitor a range of open-pit mining operations, which pose significant environmental risks worldwide. The adoption of the InSAR approach presented in this study is highly valuable, as until now, the lack of easily applicable methods for detecting mine debris has often prevented the formulation of policies to mitigate mine dust hazards that threaten the local environment and human health.

Furthermore, we emphasize the potential of this method to monitor aeolian erosion processes and the transportation of generated sediments. The absence of quantitative methods to measure aeolian erosion and its consequences has hindered the proper interpretation of geomorphological processes. We propose that the method developed in this study can

be effectively combined with existing techniques such as Structure from Motion (SfM) and InSAR phase coherence analysis to produce well-quantified observations in eroding terrain.

With the future planned InSAR missions, the advantages of this approach will become even more apparent, providing a powerful tool for environmental monitoring and risk mitigation in mining areas.

Author Contributions: Conceptualization, J.K., B.A. and A.B.; methodology, J.K. and B.A.; software, J.K.; validation, A.B. and J.K.; formal analysis, J.K.; investigation, J.K., A.B. and B.A.; resources, J.K., B.A. and A.B.; data curation, J.K. and A.B.; writing—original draft preparation, J.K.; writing—review and editing, J.K., B.A. and A.B.; visualization, J.K. All authors have read and agreed to the published version of the manuscript.

Funding: This research received no external funding.

Data Availability Statement: The data that support the findings of this study are available on request from the corresponding author.

Acknowledgments: The author would like to acknowledge the generous support provided by the Korea-Mongolia Greenbelt Project provided for the ground survey. The paper does not necessarily reflect the opinions or policies of the supporting organizations. The authors acknowledge that they relied on the hospitality and assistance of residents in the Gobi Desert during the fieldwork. The authors are immensely grateful to the editor and anonymous reviewers for their useful comments.

Conflicts of Interest: Jungrack Kim is employed by Future Vision Inc. The authors declare that they have no conflicts of interest.

References

1. Lin, C.; Tong, X.; Lu, W.; Yan, L.; Wu, Y.; Nie, C.; Chu, C.; Long, J. Environmental impacts of surface mining on mined lands, affected streams and agricultural lands in the Dabaoshan Mine region, southern China. *Land Degrad. Dev.* **2005**, *16*, 463–474. [CrossRef]
2. Wolkersdorfer, C.; Mugova, E. Effects of mining on surface water. *Encycl. Inland Waters* **2022**, *4*, 170–188.
3. Tiwary, R. Environmental impact of coal mining on water regime and its management. *Water Air Soil Pollut.* **2001**, *132*, 185–199. [CrossRef]
4. Wang, S.; Li, X.; Wang, D. Void fraction distribution in overburden disturbed by longwall mining of coal. *Environ. Earth Sci.* **2016**, *75*, 1–17. [CrossRef]
5. De Rosa, M.I. *Analysis of Mine Fires for All US Underground and Surface Coal Mining Categories: 1990–1999*; NIOSH: Cincinnati, OH, USA, 2004.
6. Kim, J.; Lin, S.-Y.; Singh, R.P.; Lan, C.-W.; Yun, H.-W. Underground burning of Jharia coal mine (India) and associated surface deformation using InSAR data. *Int. J. Appl. Earth Obs. Geoinf.* **2021**, *103*, 102524. [CrossRef]
7. Sánchez-Donoso, R.; Martín-Duque, J.F.; Crespo, E.; Higueras, P.L. Tailing's geomorphology of the San Quintín mining site (Spain): Landform catalogue, aeolian erosion and environmental implications. *Environ. Earth Sci.* **2019**, *78*, 166. [CrossRef]
8. Ferreira, M.; Furieri, B.; Santos, J.; El Moctar, A.O.; Harion, J.-L.; Valance, A.; Dupont, P.; Reis, N. An experimental and numerical study of the aeolian erosion of isolated and successive piles. *Environ. Fluid Mech.* **2020**, *20*, 123–144. [CrossRef]
9. Baruya, P. *Losses in the Coal Supply Chain*; IEA Clean Coal Centre: London, UK, 2012.
10. Perret, J.L.; Plush, B.; Lachapelle, P.; Hinks, T.S.; Walter, C.; Clarke, P.; Irving, L.; Brady, P.; Dharmage, S.C.; Stewart, A. Coal mine dust lung disease in the modern era. *Respirology* **2017**, *22*, 662–670. [CrossRef]
11. Pan, L.; Golden, S.; Assemi, S.; Sime, M.F.; Wang, X.; Gao, Y.; Miller, J. Characterization of particle size and composition of respirable coal mine dust. *Minerals* **2021**, *11*, 276. [CrossRef]
12. Liu, T.; Liu, S. The impacts of coal dust on miners' health: A review. *Environ. Res.* **2020**, *190*, 109849. [CrossRef]
13. Abbasi, B.; Wang, X.; Chow, J.C.; Watson, J.G.; Peik, B.; Nasiri, V.; Riemenschnitter, K.B.; Elahifard, M. Review of respirable coal mine dust characterization for mass concentration, size distribution and chemical composition. *Minerals* **2021**, *11*, 426. [CrossRef]
14. Amgalan, G.; Liu, G.-R.; Kuo, T.-H.; Tang-Huang, L. Correlation between dust events in Mongolia and surface wind and precipitation. *TAO Terr. Atmos. Ocean. Sci.* **2017**, *28*, 2. [CrossRef]
15. Kim, J.; Dorjsuren, M.; Zucca, C.; Purevjav, G. Mapping land degradation and sand and dust generation hotspots by spatiotemporal data fusion analysis: A case-study in the southern Gobi (Mongolia). *Land Degrad. Dev.* **2023**, *34*, 1629–1647. [CrossRef]
16. Kim, J.-R.; Lin, C.-W.; Lin, S.-Y. The Use of InSAR Phase Coherence Analyses for the Monitoring of Aeolian Erosion. *Remote Sens.* **2021**, *13*, 2240. [CrossRef]
17. Kim, J.; Dorjsuren, M.; Choi, Y.; Purevjav, G. Reconstructed aeolian surface erosion in southern Mongolia by multi-temporal InSAR phase coherence analyses. *Front. Earth Sci.* **2020**, *8*, 531104. [CrossRef]

18. Avirmed, D. Mineral resources of Mongolia as a driving force of the country. *Mong. J. Int. Aff.* **2021**, *22*, 61–66. [CrossRef]
19. Gerel, O.; Pirajno, F.; Batkhishig, B.; Dostal, J. *Mineral Resources of Mongolia*; Springer: Berlin/Heidelberg, Germany, 2021.
20. Erdenetsogt, B.-O.; Lee, I.; Bat-Erdene, D.; Jargal, L. Mongolian coal-bearing basins: Geological settings, coal characteristics, distribution, and resources. *Int. J. Coal Geol.* **2009**, *80*, 87–104. [CrossRef]
21. Tsembelsuren, B.; Hwan, Y.C.; Rong, K. Study of Coal Trade between Mongolia and China, its Effect in Mongolian Coal Market. *Eur. Res.* **2012**, *19*, 379–382.
22. Ma, Q.; Wu, J.; He, C.; Fang, X. The speed, scale, and environmental and economic impacts of surface coal mining in the Mongolian Plateau. *Resour. Conserv. Recycl.* **2021**, *173*, 105730. [CrossRef]
23. Xu, Y.; Zhang, Y.; Chen, J. Migration under economic transition and changing climate in Mongolia. *J. Arid. Environ.* **2021**, *185*, 104333. [CrossRef]
24. Gombodorj, G.; Pető, K. Impact Of The Mining And Agriculture Sector On The Mongolian Economy. *Oradea J. Bus. Econ.* **2022**, *7*, 74–85. [CrossRef]
25. Mongolia: Five Largest Mines in 2021. Available online: https://www.globaldata.com/data-insights/mining/mongolia--five-largest-mines-in-2090784/ (accessed on 1 July 2024).
26. Yagüe-Martínez, N.; Prats-Iraola, P.; Gonzalez, F.R.; Brcic, R.; Shau, R.; Geudtner, D.; Eineder, M.; Bamler, R. Interferometric processing of Sentinel-1 TOPS data. *IEEE Trans. Geosci. Remote Sens.* **2016**, *54*, 2220–2234. [CrossRef]
27. Geudtner, D.; Torres, R.; Snoeij, P.; Davidson, M.; Rommen, B. Sentinel-1 system capabilities and applications. In Proceedings of the 2014 IEEE Geoscience and Remote Sensing Symposium, Quebec City, QC, Canada, 13–18 July 2014; pp. 1457–1460.
28. Lazecký, M.; Spaans, K.; González, P.J.; Maghsoudi, Y.; Morishita, Y.; Albino, F.; Elliott, J.; Greenall, N.; Hatton, E.; Hooper, A. LiCSAR: An automatic InSAR tool for measuring and monitoring tectonic and volcanic activity. *Remote Sens.* **2020**, *12*, 2430. [CrossRef]
29. Riegler, G.; Hennig, S.; Weber, M. *Worlddem—A Novel Global Foundation Layer*; International Archives of the Photogrammetry, Remote Sensing & Spatial Information Sciences; ISPRS: Hannover, Germany, 2015.
30. Krieger, G.; Moreira, A.; Fiedler, H.; Hajnsek, I.; Werner, M.; Younis, M.; Zink, M. TanDEM-X: A satellite formation for high-resolution SAR interferometry. *IEEE Trans. Geosci. Remote Sens.* **2007**, *45*, 3317–3341. [CrossRef]
31. Bielski, C.; López-Vázquez, C.; Grohmann, C.H.; Guth, P.L.; Hawker, L.; Gesch, D.; Trevisani, S.; Herrera-Cruz, V.; Riazanoff, S.; Corseaux, A. Novel approach for ranking DEMs: Copernicus DEM improves one arc second open global topography. *IEEE Trans. Geosci. Remote Sens.* **2024**, *62*, 1–22. [CrossRef]
32. Rodell, M.; Houser, P.; Jambor, U.; Gottschalck, J.; Mitchell, K.; Meng, C.-J.; Arsenault, K.; Cosgrove, B.; Radakovich, J.; Bosilovich, M. The global land data assimilation system. *Bull. Am. Meteorol. Soc.* **2004**, *85*, 381–394. [CrossRef]
33. Muñoz-Sabater, J.; Dutra, E.; Agustí-Panareda, A.; Albergel, C.; Arduini, G.; Balsamo, G.; Boussetta, S.; Choulga, M.; Harrigan, S.; Hersbach, H. ERA5-Land: A state-of-the-art global reanalysis dataset for land applications. *Earth Syst. Sci. Data* **2021**, *13*, 4349–4383. [CrossRef]
34. Ferretti, A.; Prati, C.; Rocca, F. Nonlinear subsidence rate estimation using permanent scatterers in differential SAR interferometry. *IEEE Trans. Geosci. Remote Sens.* **2000**, *38*, 2202–2212. [CrossRef]
35. Ferretti, A.; Prati, C.; Rocca, F. Permanent scatterers in SAR interferometry. *IEEE Trans. Geosci. Remote Sens.* **2001**, *39*, 8–20. [CrossRef]
36. Kim, J.-R.; Lin, S.-Y.; Oh, J.-W. The Survey of Lava Tube Distribution in Jeju Island by Multi-Source Data Fusion. *Remote Sens.* **2022**, *14*, 443. [CrossRef]
37. Li, S.; Xu, W.; Li, Z. Review of the SBAS InSAR Time-series algorithms, applications, and challenges. *Geod. Geodyn.* **2022**, *13*, 114–126. [CrossRef]
38. Berardino, P.; Fornaro, G.; Lanari, R.; Sansosti, E. A new algorithm for surface deformation monitoring based on small baseline differential SAR interferograms. *IEEE Trans. Geosci. Remote Sens.* **2002**, *40*, 2375–2383. [CrossRef]
39. Kim, J.; Lin, S.-Y.; Singh, T.; Singh, R.P. InSAR time series analysis to evaluate subsidence risk of monumental Chandigarh City (India) and surroundings. *IEEE Trans. Geosci. Remote Sens.* **2023**, *61*, 4505715. [CrossRef]
40. Kalavrezou, I.-E.; Castro-Melgar, I.; Nika, D.; Gatsios, T.; Lalechos, S.; Parcharidis, I. Application of Time Series INSAR (SBAS) Method Using Sentinel-1 for Monitoring Ground Deformation of the Aegina Island (Western Edge of Hellenic Volcanic Arc). *Land* **2024**, *13*, 485. [CrossRef]
41. Kim, J.-R.; Lin, S.-Y.; Hong, S.; Choi, Y.-S.; Yun, H.-W. Ground deformation tracking over Mt. Baekdu: A pre-evaluation of possible magma recharge by D-InSAR analysis. *KSCE J. Civ. Eng.* **2014**, *18*, 1505–1510. [CrossRef]
42. Yunjun, Z.; Fattahi, H.; Amelung, F. Small baseline InSAR time series analysis: Unwrapping error correction and noise reduction. *Comput. Geosci.* **2019**, *133*, 104331. [CrossRef]
43. Perissin, D.; Wang, T. Repeat-pass SAR interferometry with partially coherent targets. *IEEE Trans. Geosci. Remote Sens.* **2011**, *50*, 271–280. [CrossRef]
44. Tough, J.; Blacknell, D.; Quegan, S. A statistical description of polarimetric and interferometric synthetic aperture radar data. *Proc. R. Soc. London. Ser. A Math. Phys. Sci.* **1995**, *449*, 567–589.
45. Samiei-Esfahany, S.; Martins, J.E.; Van Leijen, F.; Hanssen, R.F. Phase estimation for distributed scatterers in InSAR stacks using integer least squares estimation. *IEEE Trans. Geosci. Remote Sens.* **2016**, *54*, 5671–5687. [CrossRef]

46. Yu, C.; Li, Z.; Penna, N.; Crippa, P. Generic atmospheric correction online service for InSAR (GACOS). In Proceedings of the EGU General Assembly Conference Abstracts, Vienna, Austria, 8–13 April 2018; p. 11007.
47. De Zan, F.; Zonno, M.; Lopez-Dekker, P. Phase inconsistencies and multiple scattering in SAR interferometry. *IEEE Trans. Geosci. Remote Sens.* **2015**, *53*, 6608–6616. [CrossRef]
48. Biggs, J.; Wright, T.; Lu, Z.; Parsons, B. Multi-interferogram method for measuring interseismic deformation: Denali Fault, Alaska. *Geophys. J. Int.* **2007**, *170*, 1165–1179. [CrossRef]
49. De Zan, F.; Gomba, G. Vegetation and soil moisture inversion from SAR closure phases: First experiments and results. *Remote Sens. Environ.* **2018**, *217*, 562–572. [CrossRef]
50. Zwieback, S.; Hensley, S.; Hajnsek, I. Assessment of soil moisture effects on L-band radar interferometry. *Remote Sens. Environ.* **2015**, *164*, 77–89. [CrossRef]
51. Kim, J. Tracing Archaeological Places via the Context of Paleo Geomorphic Footprints Using SAR/InSAR Data Fusion: A Case on Southern Mesopotamia. *Remote Sens.* **2023**, *15*, 1636. [CrossRef]
52. Yun, H.-W.; Kim, J.-R.; Choi, Y.-S.; Lin, S.-Y. Analyses of time series InSAR signatures for land cover classification: Case studies over dense forestry areas with L-band SAR images. *Sensors* **2019**, *19*, 2830. [CrossRef]
53. Chen, C.W.; Zebker, H.A. Phase unwrapping for large SAR interferograms: Statistical segmentation and generalized network models. *IEEE Trans. Geosci. Remote Sens.* **2002**, *40*, 1709–1719. [CrossRef]
54. Fuhrmann, T.; Garthwaite, M.C. Resolving three-dimensional surface motion with InSAR: Constraints from multi-geometry data fusion. *Remote Sens.* **2019**, *11*, 241. [CrossRef]
55. Yun, H.-W.; Kim, J.-R.; Yoon, H.; Choi, Y.; Yu, J. Seismic surface deformation risks in industrial hubs: A case study from Ulsan, Korea, using DInSAR time series analysis. *Remote Sens.* **2019**, *11*, 1199. [CrossRef]
56. Chang, C.-I. Spectral information divergence for hyperspectral image analysis. In Proceedings of the IEEE 1999 International Geoscience and Remote Sensing Symposium. IGARSS'99 (Cat. No. 99CH36293), Hamburg, Germany, 28 June–2 July 1999; pp. 509–511.
57. Sazib, N.; Mladenova, I.; Bolten, J. Leveraging the Google Earth Engine for drought assessment using global soil moisture data. *Remote Sens.* **2018**, *10*, 1265. [CrossRef]
58. Wang, L.; Qu, J.J. NMDI: A normalized multi-band drought index for monitoring soil and vegetation moisture with satellite remote sensing. *Geophys. Res. Lett.* **2007**, *34*. [CrossRef]
59. Fang, H.; Baret, F.; Plummer, S.; Schaepman-Strub, G. An overview of global leaf area index (LAI): Methods, products, validation, and applications. *Rev. Geophys.* **2019**, *57*, 739–799. [CrossRef]
60. Stein, A.F.; Draxler, R.R.; Rolph, G.D.; Stunder, B.J.; Cohen, M.D.; Ngan, F. NOAA's HYSPLIT atmospheric transport and dispersion modeling system. *Bull. Am. Meteorol. Soc.* **2015**, *96*, 2059–2077. [CrossRef]
61. Draxler, R.R.; Hess, G. An overview of the HYSPLIT_4 modelling system for trajectories. *Aust. Meteorol. Mag.* **1998**, *47*, 295–308.
62. Warner, M.S. Introduction to PySPLIT: A Python toolkit for NOAA ARL's HYSPLIT model. *Comput. Sci. Eng.* **2018**, *20*, 47–62. [CrossRef]
63. Sauermann, G.; Kroy, K.; Herrmann, H.J. Continuum saltation model for sand dunes. *Phys. Rev. E* **2001**, *64*, 031305. [CrossRef]
64. Zhang, P.; Sherman, D.J.; Li, B. Aeolian creep transport: A review. *Aeolian Res.* **2021**, *51*, 100711. [CrossRef]
65. Topić, N.; Žitnik, M. Fugitive Dust Emissions from a Coal-, Iron Ore-and Hydrated Alumina Stockpile. In *Air Pollution-Monitoring, Modelling and Health*; IntechOpen: London, UK, 2012.
66. Darmenova, K.; Sokolik, I.N.; Shao, Y.; Marticorena, B.; Bergametti, G. Development of a physically based dust emission module within the Weather Research and Forecasting (WRF) model: Assessment of dust emission parameterizations and input parameters for source regions in Central and East Asia. *J. Geophys. Res. Atmos.* **2009**, *114*. [CrossRef]
67. Shao, Y. *Physics and Modelling of Wind Erosion*; Springer: Berlin/Heidelberg, Germany, 2008.
68. Marticorena, B.; Bergametti, G. Modeling the atmospheric dust cycle: 1. Design of a soil-derived dust emission scheme. *J. Geophys. Res. Atmos.* **1995**, *100*, 16415–16430. [CrossRef]
69. Krinke, T.J.; Deppert, K.; Magnusson, M.H.; Schmidt, F.; Fissan, H. Microscopic aspects of the deposition of nanoparticles from the gas phase. *J. Aerosol Sci.* **2002**, *33*, 1341–1359. [CrossRef]
70. Zhou, Q.; Qin, B. Coal dust suppression based on water mediums: A review of technologies and influencing factors. *Fuel* **2021**, *302*, 121196. [CrossRef]
71. Ma, Q.; Nie, W.; Yang, S.; Xu, C.; Peng, H.; Liu, Z.; Guo, C.; Cai, X. Effect of spraying on coal dust diffusion in a coal mine based on a numerical simulation. *Environ. Pollut.* **2020**, *264*, 114717. [CrossRef] [PubMed]
72. Ren, T.X.; Plush, B.; Aziz, N. Dust controls and monitoring practices on Australian longwalls. *Procedia Eng.* **2011**, *26*, 1417–1429. [CrossRef]
73. Asian Development Bank. *Demand in the Desert Mongolia's Water–Energy–Mining Nexus*; Asian Development Bank: Metro Manila, Philippines, 2016.

Disclaimer/Publisher's Note: The statements, opinions and data contained in all publications are solely those of the individual author(s) and contributor(s) and not of MDPI and/or the editor(s). MDPI and/or the editor(s) disclaim responsibility for any injury to people or property resulting from any ideas, methods, instructions or products referred to in the content.